

FORMATION PROCESS OF THE CIRCUMSTELLAR DISK: LONG-TERM SIMULATIONS IN THE MAIN ACCRETION PHASE OF STAR FORMATION

MASAHIRO N. MACHIDA¹, SHU-ICHIRO INUTSUKA², AND TOMOAKI MATSUMOTO³

¹ National Astronomical Observatory of Japan, Mitaka, Tokyo 181-8588, Japan; masahiro.machida@nao.ac.jp

² Department of Physics Nagoya University Furo-cho, Chikusa-ku Nagoya, Aichi 464-8602, Japan; inutsuka@nagoya-u.jp

³ Faculty of Humanity and Environment, Hosei University, Fujimi, Chiyoda-ku, Tokyo 102-8160, Japan; matsu@hosei.ac.jp

Received 2010 January 9; accepted 2010 September 21; published 2010 November 10

ABSTRACT

The formation and evolution of the circumstellar disk in unmagnetized molecular clouds is investigated using three-dimensional hydrodynamic simulations from the prestellar core until the end of the main accretion phase. In collapsing cloud cores, the first (adiabatic) core with a size of $\gtrsim 3$ AU forms prior to the formation of the protostar. At its formation, the first core has a thick disk-like structure and is mainly supported by the thermal pressure. After the protostar formation, it decreases the thickness gradually and becomes supported by the centrifugal force. We found that the first core is a precursor of the circumstellar disk with a size of > 3 AU. This means that unmagnetized protoplanetary disk smaller than < 3 AU does not exist. Reflecting the thermodynamics of the collapsing gas, at the protostar formation epoch, the first core (or the circumstellar disk) has a mass of $\sim 0.005\text{--}0.1 M_{\odot}$, while the protostar has a mass of $\sim 10^{-3} M_{\odot}$. Thus, just after the protostar formation, the circumstellar disk is about 10–100 times more massive than the protostar. In the main accretion phase that lasts for $\sim 10^5$ yr, the circumstellar disk mass initially tends to dominate the protostellar mass. Such a massive disk is unstable to gravitational instability and tends to show fragmentation. Our calculations indicate that the low-mass companions may form in the circumstellar disk in the main accretion phase. In addition, the mass accretion rate onto the protostar shows a strong time variability that is caused by the torque from the low-mass companions and/or the spiral arms in the circumstellar disk. Such variability provides an important signature for detecting the substellar mass companion in the circumstellar disk around very young protostars.

Key words: accretion, accretion disks – brown dwarfs – ISM: clouds – protoplanetary disks – stars: formation – stars: low-mass

Online-only material: color figures

1. INTRODUCTION

We believe that stars are born with a circumstellar disk (see Meyer et al. 2007; Najita et al. 2007; Watson et al. 2007, and references therein). The formation of the circumstellar disk is coupled with “the angular momentum problem” which is a serious problem in the star formation process, and the dynamics of disks may determine the mass accretion rate onto the protostar that determines the final stellar mass. In addition, planets are considered to form in the circumstellar (or protoplanetary) disk, and their formation process strongly depends on disk properties such as disk size and mass. Thus, the formation and evolution of the circumstellar disk can provide a significant clue to star and planet formation.

Stars form in molecular clouds that have an angular momentum (Arquilla & Goldsmith 1986; Goodman et al. 1993; Caselli et al. 2002). Thus, the appearance of a circumstellar disk is a natural consequence of the star formation process when the angular momentum is conserved in the collapsing cloud core. In addition, observations have shown the existence of circumstellar disks around the protostar (e.g., Watson et al. 2007; Dutrey et al. 2007; Meyer et al. 2007). Numerous observations indicate that circumstellar disks around Classes I and II protostars have sizes of $\sim 10\text{--}1000$ AU and masses of $\sim 10^{-3}\text{--}0.1 M_{\odot}$ (e.g., Calvet et al. 2000; Natta et al. 2000). However, these correspond to phases long after their formation. Because the formation site of the circumstellar disk and protostar are embedded in a dense infalling envelope, we cannot directly observe newborn or very young circumstellar disks (and protostars). Thus, we only

observe the circumstellar disks long after their formation, i.e., around the Class I or II protostar phase.

Observations also indicate that a younger protostar has a massive circumstellar disk (Natta et al. 2000; Meyer et al. 2007). Recently, Enoch et al. (2009) observed a massive disk with $M_{\text{disk}} \sim 1 M_{\odot}$ around Class 0 sources, indicating that this massive disk can be present early in the main accretion phase. However, unfortunately, observation cannot determine the real sizes of circumstellar disks, and how and when they form. Therefore, we cannot understand the formation process of the circumstellar disk by observations. Theoretical approach and numerical simulation are necessary to investigate the formation and evolution of the circumstellar disk.

Theoretically, the star formation process can be divided into two phases, i.e., the early collapse phase and main accretion phase. The molecular cloud cores that are star cradles have a number density of $n \sim 10^4\text{--}10^6 \text{ cm}^{-3}$. In the early collapse phase, the gas in the molecular cloud core continues to collapse until the protostar formation at $n \sim 10^{21} \text{ cm}^{-3}$. The protostar at its formation has a mass of $M_{\text{ps}} \sim 10^{-3} M_{\odot}$ which corresponds to the Jovian mass (Larson 1969; Masunaga & Inutsuka 2000). In the main accretion phase, the protostar acquires almost all its mass by gas accretion to reach $\sim 1 M_{\odot}$. In this paper, we define “the early collapse phase” as the period before the protostar formation, while “the main accretion phase” is defined as the period until gas accretion onto the protostellar system (protostar and circumstellar disk) almost halts after the protostar formation. In general, it is considered that the circumstellar disk gradually increases its mass and size in the main accretion phase

that is successively connected to the early collapse phase. Thus, to understand the formation and early evolution of circumstellar disks, we should consider both the early collapse and main accretion phases; we need a self-consistent calculation from the collapse of the molecular cloud core until the end of the main accretion phase through the protostar formation.

However, to investigate the formation and evolution of circumstellar disks in numerical simulations, we need a very long-term calculation with a sufficient spatial resolution, in which we should calculate the evolution of the protostellar system at least for the time comparable to the free-fall timescale of the initial cloud core, i.e., $\gtrsim 10^4$ – 10^5 yr after the protostar formation. In addition, we should resolve spatial scale length down to at least ~ 1 AU. Reflecting the thermodynamics of the collapsing gas, the two nested cores with typical spatial scales appear in the early collapse phase (Larson 1969; Masunaga & Inutsuka 2000). The inner core (the so-called second adiabatic core) corresponds to the protostar that has a size of $\sim 1 R_\odot$, while the outer core that is called the first (adiabatic) core has a size of ~ 1 – 10 AU (for details, see Section 3.1.1). Inutsuka et al. (2010) proposed that the circumstellar disk that originates in the first core formed in the early collapse phase (see also Bate 1998). Thus, to investigate the formation of the circumstellar disk, we have to resolve the first core spatially; we need a spatial resolution of $\lesssim 1$ AU at least. Moreover, we need a three-dimensional calculation to properly treat the angular momentum transport in the circumstellar disk.

So far, many studies of star formation in the collapsing cloud mainly focused only on the early collapse phase (e.g., Bodenheimer et al. 2000; Goodwin et al. 2007). To investigate the formation and evolution of the circumstellar disk, we have to calculate the early collapse and subsequent main accretion phases. However, since such a calculation requires a huge amount of CPU time, only a few studies reported the formation of the circumstellar disk in the collapsing cloud core including the main accretion phase. Kratter et al. (2010) investigated the formation of the circumstellar disk with sub-AU resolution under the isothermal approximation and showed frequent fragmentation of the disk. Walch et al. (2009) also studied the circumstellar disk formation in the collapsing cloud core with a slightly coarser spatial resolution of 2 AU approximating the radiative cooling with adiabatic equation of state and showed the properties of the circumstellar disk.

In this study, using three-dimensional simulation adopting a barotropic equation of state with a higher spatial resolution than in previous studies, the evolution of the unmagnetized collapsing cloud cores is investigated until the gas accretion onto the protostar and circumstellar disk almost halts. In three dimensions, we first calculate the evolution of the circumstellar disk by the end of the main accretion phase. Although the circumstellar disk formation in the collapsing cloud may be investigated with a radiation-hydrodynamics code, it is very difficult to execute such a calculation even with current supercomputers because it takes a huge amount of CPU time. Thus, to trace the gas thermodynamics, we chose a barotropic equation of state that is used even in recent two-dimensional simulations of the circumstellar disk formation (e.g., Vorobyov & Basu 2007; Vorobyov 2009). The structure of the paper is as follows. The framework of our models and the numerical method are given in Section 2. The numerical results are presented in Section 3. We discuss the fragmentation condition of the circumstellar disk and implication of the planet formation in Section 4 and summarize our results in Section 5.

2. MODEL

2.1. Basic Equations and Initial Settings

To study the evolution of collapsing gas clouds and circumstellar disks, we solve the equations of hydrodynamics including self-gravity:

$$\frac{\partial \rho}{\partial t} + \nabla \cdot (\rho \mathbf{v}) = 0, \quad (1)$$

$$\rho \frac{\partial \mathbf{v}}{\partial t} + \rho (\mathbf{v} \cdot \nabla) \mathbf{v} = -\nabla P - \rho \nabla \phi, \quad (2)$$

where ρ , \mathbf{v} , and P denote the density, velocity, and pressure, respectively. Since the protostar is modeled using the sink (see Section 2.2), the gravitational potential is composed of two parts:

$$\phi = \phi_{\text{gas}} + \phi_{\text{ps}}. \quad (3)$$

The first term is the self-gravity of the gas, $\nabla^2 \phi_{\text{gas}} = 4\pi G \rho$, while the second term is the gravitational potential of the protostar, $\phi_{\text{ps}} = -GM_{\text{ps}}/r$, where M_{ps} is the mass of the protostar. To mimic the temperature evolution calculated by Masunaga & Inutsuka (2000), we adopt the piecewise polytropic equation of state (see Machida et al. 2007) as

$$P = c_{s,0}^2 \rho \left[1 + \left(\frac{\rho}{\rho_c} \right)^{2/5} \right], \quad (4)$$

where $c_{s,0} = 190 \text{ m s}^{-1}$ and $\rho_c = 3.84 \times 10^{-14} \text{ g cm}^{-3}$ ($n_c = 10^{10} \text{ cm}^{-3}$).

As the initial state, we take a spherical cloud with critical Bonnor–Ebert (BE) density profile, in which the uniform density is adopted outside the sphere ($r > R_c$). For the BE density profile, we adopt the central density of $n_c = 6 \times 10^5 \text{ cm}^{-3}$ and isothermal temperature of $T = 10 \text{ K}$. For these parameters, the critical BE radius is $R_c = 6.2 \times 10^3 \text{ AU}$. To promote contraction, we increase the density by a factor of $f = 1.68$, where f is the density enhancement factor that represents the stability of the initial cloud. With $f = 1.68$, the initial cloud has (negative) gravitational energy twice that of thermal energy. Thus, the central density of the initial sphere is $n_{c,\text{ini}} = 10^6 \text{ cm}^{-3}$, while the ambient density is $n_{\text{amb}} = 7.2 \times 10^4 \text{ cm}^{-3}$. We add the $m = 2$ mode non-axisymmetric density perturbation to the initial core. Then, the density profile of the core is described as

$$\rho(r) = \begin{cases} \rho_{\text{BE}}(r)(1 + \delta_\rho) f & \text{for } r < R_c, \\ \rho_{\text{BE}}(R_c)(1 + \delta_\rho) f & \text{for } r \geq R_c, \end{cases} \quad (5)$$

where $\rho_{\text{BE}}(r)$ is the density distribution of the critical BE sphere and δ_ρ is the axisymmetric density perturbation. For the $m = 2$ mode, we chose

$$\delta_\rho = A_\phi (r/R_c)^2 \cos 2\phi, \quad (6)$$

where $A_\phi (= 0.01)$ represents the amplitude of the perturbation. The radial dependence is chosen so that the density perturbation remains regular at the origin ($r = 0$) at one time step after the initial stage. This perturbation ensures that the center of gravity is always located at the origin. The mass within $r < R_c$ is $M = 1 M_\odot$. The gravitational force is ignored outside the

Table 1
Model Parameters and Calculation Results

Model	β_0	Ω_0 (s ⁻¹)	M_{ps} (M_\odot)	M_{disk} (M_\odot)	$M_{\text{red}}^{\text{a}}$ (M_\odot)	μ^{b}	r_{disk} (AU)	$t_{\text{frag}}^{\text{c}}$ (yr)	M_{frag} (M_\odot)	R_{sep} (AU)
1	5×10^{-2}	2.7×10^{-13}	0.072	57.3
2	3×10^{-2}	2.1×10^{-13}	0.14	0.09	0.77	0.64	210	2.0×10^3	0.061	94.2
3	10^{-2}	1.2×10^{-13}	0.35	0.58	0.07	1.66	520
4	5×10^{-3}	8.6×10^{-14}	0.43	0.51	0.06	1.19	409
5	3×10^{-3}	6.6×10^{-14}	0.48	0.49	0.03	1.02	270	3.4×10^4	0.058	21.1
6	10^{-3}	3.8×10^{-14}	0.47	0.42	0.11	0.89	202	1.5×10^4	0.037	11.7
7	3×10^{-4}	2.1×10^{-14}	0.51	0.38	0.11	0.74	152	9.8×10^3	0.031	7.2
8	10^{-4}	1.2×10^{-14}	0.52	0.34	0.14	0.65	117	7.7×10^3	0.049	7.8
9	3×10^{-5}	6.6×10^{-15}	0.80	0.16	0.04	0.20	29	2.0×10^4	0.019	7.1
10	10^{-5}	3.8×10^{-15}	0.90	0.08	0.02	0.09	23

Notes.

^a Disk-to-protostar mass ratio ($= M_{\text{disk}}/M_{\text{ps}}$).

^b Residual mass [$= (M_{\text{ini}} - M_{\text{ps}} - M_{\text{disk}})$].

^c Fragmentation epoch after the protostar formation.

host cloud ($r > R_c$) to mimic a stationary interstellar medium. Initially, the cloud rotates rigidly with angular velocity Ω_0 around the z -axis.

In this study, we focus on the formation and evolution of the circumstellar disk. Properties of the circumstellar disk are expected to depend strongly on the rotation rate of molecular cloud cores because the initial structure of the disk should depend on angular momentum distribution. Thus, we parameterized the rotation rate of the initial cloud and fixed other parameters such as the thermal energy and total mass of the cloud for simplicity. In general, the rotation rate of the cloud can be described by a simple parameter β_0 that is defined as

$$\beta_0 = \frac{E_{\text{rot}}}{|E_{\text{grav}}|}, \quad (7)$$

where E_{rot} and E_{grav} are the rotational and gravitational energy inside the initial cloud ($r < R_c$), respectively (for more details, see Matsumoto & Hanawa 2003). We calculated 10 models with different β_0 . Model names, initial angular velocities Ω_0 , and β_0 are summarized in Table 1. In this study, we limit β_0 in the range $\beta_0 \leq 0.05$ to avoid fragmentation before the protostar formation, while observations showed that molecular cloud cores have $10^{-4} < \beta_0 < 0.07$ with a typical value of $\beta_0 \sim 0.02$ (Caselli et al. 2002). As shown in Matsumoto & Hanawa (2003) and Machida et al. (2008), fragmentation occurs in the collapsing cloud before the protostar formation when $\beta_0 \gtrsim 10^{-3} - 10^{-2}$, and a binary system appears. To focus on the evolution of the circumstellar disk around a single protostar, we adopted lower values of β_0 .

2.2. Sink Cells

To realize a long-term calculation of the circumstellar disk, we adopt a sink at the center of the cloud. We start the calculation without a sink and calculate the cloud evolution for the prestellar gas-collapsing phase without the sink. Later we identify the protostar formation in the collapsing cloud core when the number density exceeds $n > n_{\text{thr}}$ at the cloud center, where n_{thr} is the threshold density for our modeling. After the protostar formation, we calculate the cloud evolution with the sink.

To model the protostar, we adopt a fixed sink with a radius of 1 AU composed of sink cells only around the center of the computational domain. Since we add only $m = 2$ density perturbation as described in Section 2.1, the protostar (or the center of gravity) does not move and remains at the center

of the computational domain during the calculation. In the region $r < r_{\text{sink}} = 1$ AU, gas having a number density of $n > n_{\text{thr}} = 10^{13} \text{ cm}^{-3}$ is removed from the computational domain and added to the protostar as a gravitating mass in each time step (Machida et al. 2009). Inside the sink, we do not change the flow velocity. We have confirmed that results do not change even if all the angular momentum inside the sink is removed at each time step.

When the gas density exceeds $n \gtrsim 10^{15} - 10^{16} \text{ cm}^{-3}$, the second collapse begins in the collapsing cloud and the protostar forms (Larson 1969; Masunaga & Inutsuka 2000). In the main accretion phase, such high-density gas accretes onto the protostar for a very short duration (< 1 yr) owing to the dissociation of the molecule hydrogen. Thus, we expect that all the gas with sufficiently high density around the protostar accretes onto the protostar (e.g., Bate 1998; Whitehouse & Bate 2006; Stamatellos et al. 2007). In addition, Bate (1998) and Machida et al. (2008) showed that fragmentation does not occur in the high-density region $n > 10^{13} \text{ cm}^{-3}$ of unmagnetized cloud (see also Matsumoto & Hanawa 2003; Hennebelle & Teyssier 2008). Thus, we may assume that all the gas exceeding $n > 10^{13} \text{ cm}^{-3}$ accretes onto the protostar without further fragmentation. For these reasons, we adopt $n_{\text{thr}} = 10^{13} \text{ cm}^{-3}$ as the threshold density.

To calculate over a large spatial scale, the nested grid method is adopted (for details, see Machida et al. 2005b, 2006). Each level of a rectangular grid has the same number of cells, $128 \times 128 \times 16$. The calculation is first performed with five grid levels ($l = 1-5$). The box size of the coarsest grid $l = 1$ is chosen to be $2^5 R_c$. Thus, a grid of $l = 1$ has a box size of 1.97×10^5 AU. A new finer grid is generated before the Jeans condition is violated. The maximum level of grids is restricted to $l_{\text{max}} \leq 12$. The $l = 12$ grid has a box size of 48 AU and cell width of 0.3 AU. With this method, we cover five orders of magnitude in spatial scale.

3. RESULTS

We investigated the cloud evolution and the circumstellar disk formation with different initial rotational energies, β_0 . In the following section, we show the cloud evolution and formation process of the circumstellar disk for two typical models (model 6 and 3). Then, we compare the properties of circumstellar disks in clouds with different rotational energies.

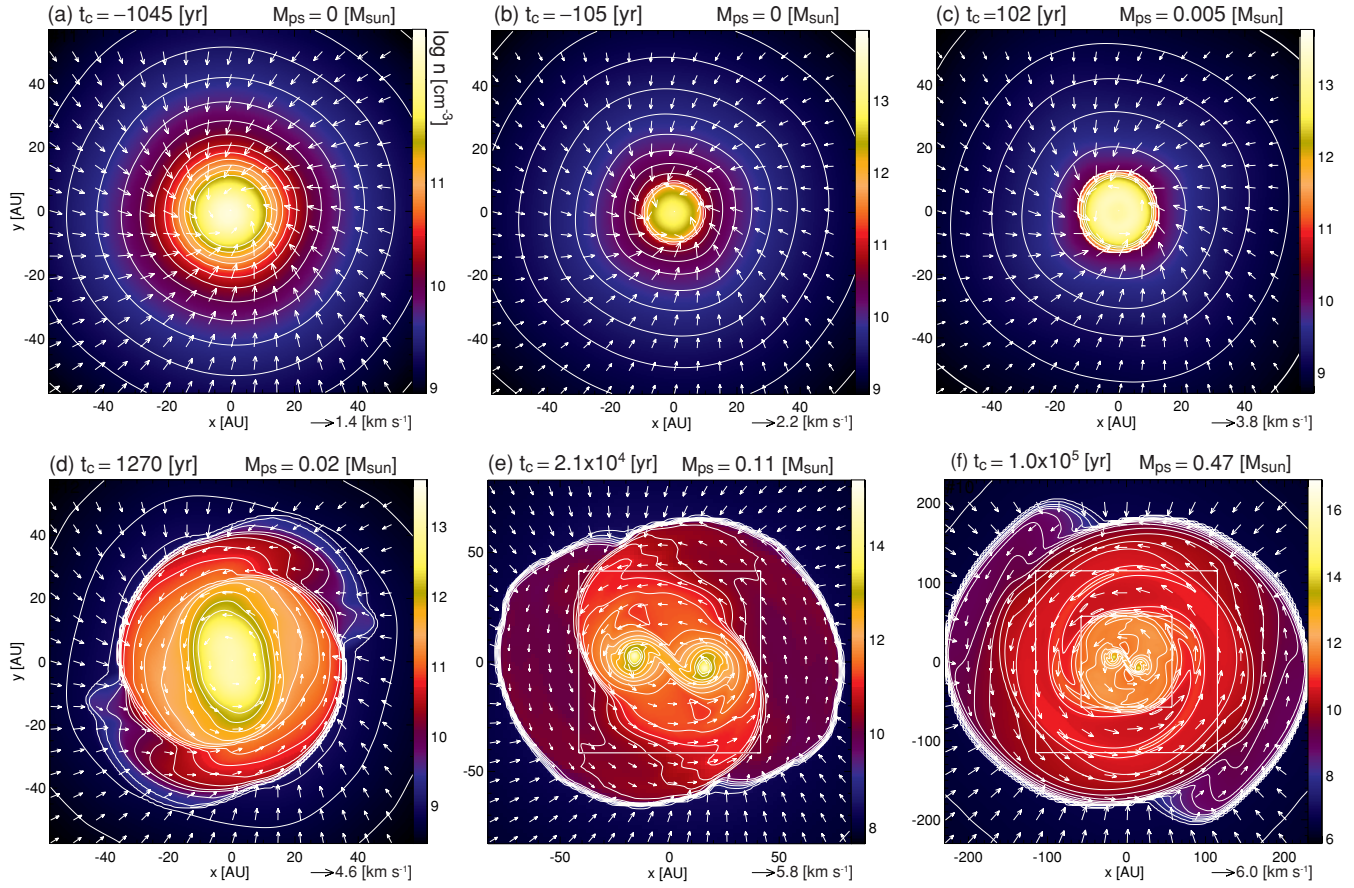


Figure 1. Evolution of the circumstellar disk for model 6 ($\beta_0 = 10^{-3}$). The density (color scale and contours) and velocity (arrows) distributions on the equatorial ($z = 0$) plane are plotted. The spatial scale is different for each panel. The time elapsed after the protostar formation (t_c) and protostellar mass (M_{ps}) are shown in the upper part of each panel.

(A color version of this figure is available in the online journal.)

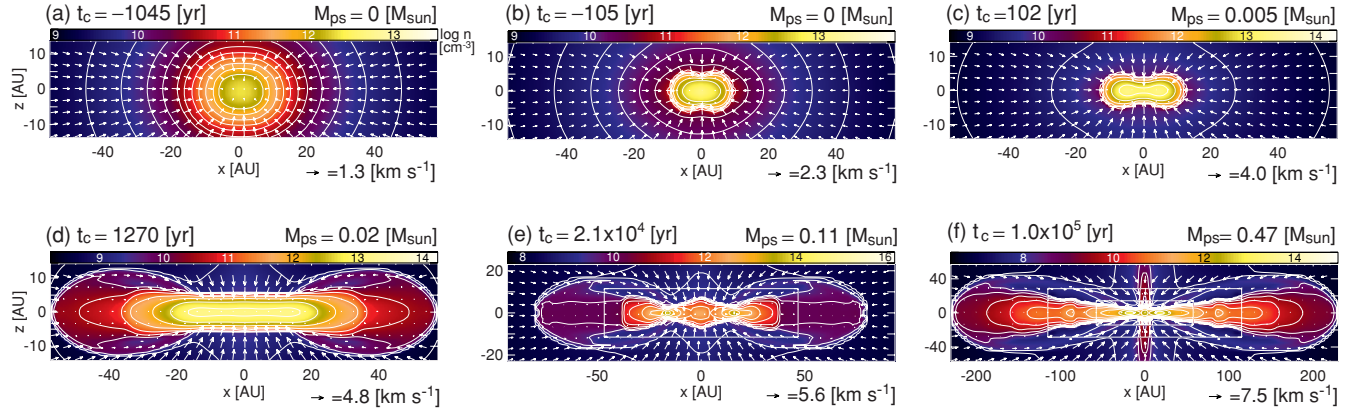


Figure 2. Density (color scale and contours) and velocity (arrows) distributions for the same model as in Figure 1 (model 6; $\beta_0 = 10^{-3}$) are plotted on the cross section of the $y = 0$ plane at the same epochs as in Figure 1.

(A color version of this figure is available in the online journal.)

3.1. Typical Models

3.1.1. Cloud with $\beta_0 = 10^{-3}$

Figures 1 and 2 show the time sequence around the center of the cloud before (panels (a) and (b)) and after (panels (c)–(f)) the protostar formation for the model with $\beta_0 = 10^{-3}$ (model 6). As denoted in Section 2.1, we define the protostar formation epoch ($t_c = 0$) as the time when the maximum density reaches $n = 10^{13}$ cm⁻³. In these figures, the time after the protostar

formation (t_c) and protostellar mass (M_{ps}) are described in each panel. The protostellar mass M_{ps} is derived as the mass falling into the sink.

Panels (a) and (b) in these figures indicate the formation of the disk-like structure before the protostar formation. To clearly define the disk, we used the ratio of the radial to azimuthal velocity $R_v (= |v_r/v_\phi|)$. Figure 3 shows the density distribution (a), the ratio of the radial to azimuthal velocity (b), and the distribution of the radial (c), and azimuthal (d) velocities against

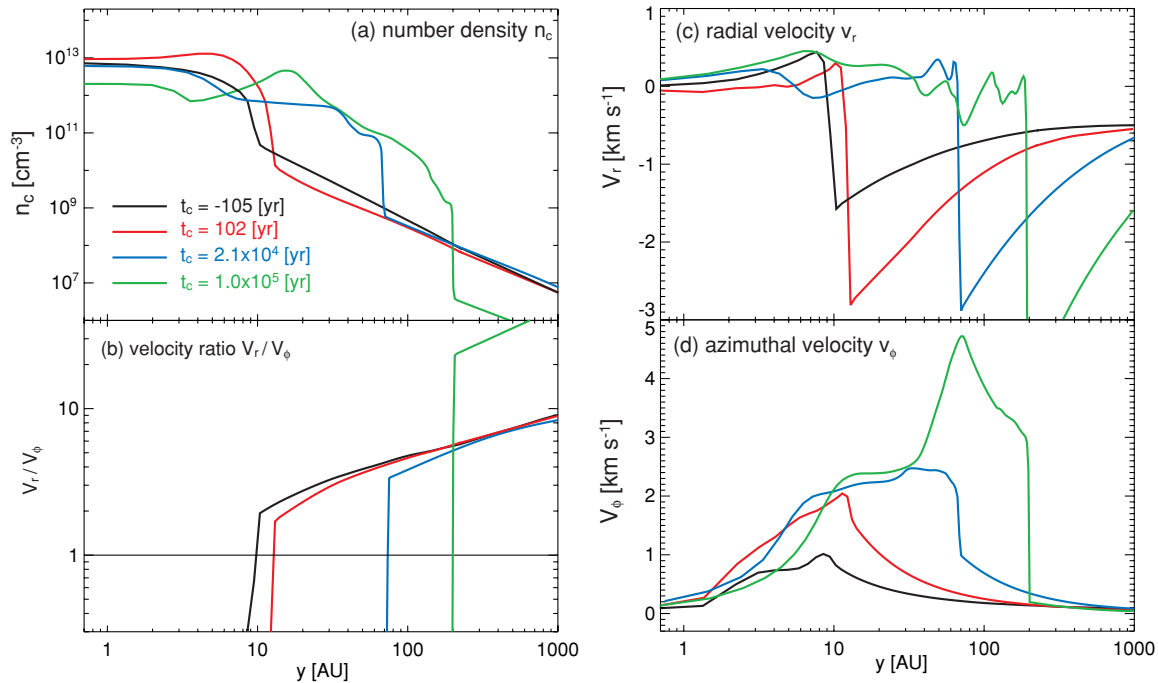


Figure 3. Radial distribution of (a) number density n_c , (b) ratio of the radial to the azimuthal velocity $R_v (= v_r/v_\phi)$, (c) radial velocity v_r , and (d) azimuthal velocity (v_ϕ) at different epochs in model 6 ($\beta_0 = 10^{-3}$). In panel (b), the velocity ratio R_v inside the disk is not displayed to emphasize the disk surface. (A color version of this figure is available in the online journal.)

the distance from the protostar along the y -axis. In Figure 3, these values for four different epochs corresponding to panels (b), (c), (e), and (f) of Figures 1 and 2 are plotted. Comparison of Figures 1 and 2 with Figure 3(a) indicates that the shock front corresponds to the disk surface. Thus, the disk-like structure is enclosed by the shock. In Figure 3(a), fine structures inside the shock surface at $t_c = 2.1 \times 10^4$ yr and at $t_c = 1.0 \times 10^5$ yr correspond to spiral density waves. Figure 3(c) shows a sudden rise of the radial velocity at the shock front. In addition, Figure 3(d) shows a large azimuthal velocity inside or near the shock front (i.e., inside or near the disk). Figures 3(c) and (d) indicate that the gas rapidly falls into the center of the cloud with a slow rotation outside the disk, while the radial velocity slows and azimuthal velocity dominates inside the disk. Therefore, the ratio of the radial to azimuthal velocity shows a sudden drop at the disk surface as shown in Figure 3(b). Note that, in Figure 3(b), to emphasize the disk surface, the velocity ratio R_v inside the disk is not displayed. As a result, the velocity ratio R_v is a good indicator for determining the disk.

In this paper, to determine the disk, we estimated the velocity ratio $R_v (= v_r/v_\phi)$ in each cell and specified the most distant cell having $R_v < 1$ from the center of the cloud. Then, we defined the disk radius r_{disk} as the distance of the cell furthest from the origin, and the disk boundary density $\rho_{\text{d,b}}$ as the density of the most distant cell. Finally, we defined the disk that has a density of $\rho > \rho_{\text{d,b}}$. Thus, in our definition, the region inside the rapid drop of R_v corresponds to the disk in Figure 3(b). Comparison of Figure 3(b) with Figures 1–3(a) indicates that this definition of the disk corresponds well to the real size of the disk in simulation.

Figure 2 shows that a thick disk-like structure formed before the protostar formation (Figures 2(a) and (b)) transforms into a sufficiently thin disk after the protostar formation (Figures 2(c)–(f)). As described in Section 1, theoretically, the star formation process can be divided into two phases: the

early collapse phase (or the early phase of the star formation) and the main accretion phase (or the later phase of the star formation). The early collapse phase was investigated in detail by Larson (1969) and Masunaga & Inutsuka (2000). Here, we briefly describe this. After the gas collapse is initiated in the molecular cloud core, the collapsing gas obeys the isothermal equation of state with temperature of ~ 10 K for $n_c \lesssim 10^{10} \text{ cm}^{-3}$ (isothermal phase). Then, the cloud collapses adiabatically ($10^{10} \lesssim n_c \lesssim 10^{16}$; adiabatic phase) and a quasi-static core (i.e., the first core) forms during the adiabatic phase. After central density reaches $n_c \simeq 10^{16} \text{ cm}^{-3}$, the equation of state becomes soft, reflecting the dissociation of hydrogen molecules at $T \simeq 2 \times 10^3$ K, and the gas collapses rapidly again, i.e., the second collapse begins. Finally, when the gas density reaches $n_c \simeq 10^{21} \text{ cm}^{-3}$, the gas collapse stops and the protostar (or the second core) forms. At this epoch, the early collapse phase ends and the main accretion phase begins. In the main accretion phase, Masunaga & Inutsuka (2000) expected that the first core without angular momentum disappears in ~ 10 yr after the protostar formation, while Saigo & Tomisaka (2006) pointed out that the first core with angular momentum does not disappear in such a short duration because the first core is supported by the rotation. Thus, we can expect that the rotating first core formed in the early collapse phase becomes the circumstellar disk in the main accretion phase. In the main accretion phase, the gas with the angular momentum continues to accrete onto the first core (or the circumstellar disk).

Figure 2 clearly shows that the first core becomes the circumstellar disk in the main accretion phase; the first core is a precursor of the circumstellar disk. The region enclosed by the shock in Figures 1(a) and 2(a) corresponds to the first core that is formed after the gas becomes adiabatic. Figures 2(b)–(e) show that the first core (or the circumstellar disk) gradually becomes thinner with time. Finally, a sufficiently thin disk appears as shown in Figure 2(f). Figure 3(b) shows that the disk has a

radius of ~ 10 AU before protostar formation. The disk extends up to ~ 200 AU for $t_c \sim 10^5$ yr in the main accretion phase. In addition, 89% of the total mass (i.e., 89% of the initial host cloud mass) accretes onto the protostar and circumstellar disk system by this epoch ($t_c \lesssim 10^5$ yr; see Table 1).

In summary, when we defined the circumstellar disk as the rotating disk around the protostar, the circumstellar disk with a size of ~ 3 – 40 AU is already formed before the protostar formation. This disk size at protostar formation corresponds to that of the first core with rotation (Matsumoto & Hanawa 2003; Saigo & Tomisaka 2006). Therefore, the circumstellar disk has a minimum size of ~ 3 AU which implies that we cannot observe a disk with $\lesssim 3$ AU even around very young protostars.

As shown in Figure 1, fragmentation occurs and two clumps form in the circumstellar disk $\sim 1.5 \times 10^4$ yr after the protostar formation. At the fragmentation epoch, the protostellar mass is $M_{ps} \sim 0.1 M_\odot$, while the disk mass is $M_{disk} \sim 0.18 M_\odot$. Thus, the disk is 1.8 times more massive than the protostar. As shown in Larson (1969) and Masunaga et al. (1998), at the protostar formation epoch, the protostar only has a mass of $\sim 10^{-3} M_\odot$ that corresponds to Jovian mass. This Jovian mass protostar acquires its mass by gas accretion for $\sim 10^5$ – 10^6 yr to reach solar mass. On the other hand, the first core has a mass of ~ 0.01 – $0.1 M_\odot$ (Matsumoto & Hanawa 2003). The masses of the protostar and first core correspond to the Jeans mass at their formation epoch. Figures 1–3 show that the first core evolves directly into the circumstellar disk through the early collapse to the main accretion phases. Thus, during the early main accretion phase, the circumstellar disk is more massive than the protostar, as described in Inutsuka et al. (2010). Since such a massive disk is gravitationally unstable, fragmentation tends to occur (Toomre 1964). In this model, at the end of the calculation, each fragment is gravitationally bound and has a mass of $\sim 0.037 M_\odot$ with ~ 12 AU of separation between the central protostar and fragment.

In this study, we try to describe fragmentation in the circumstellar disk with the Jeans condition (Truelove et al. 1997), while we need a higher spatial resolution to calculate the evolution of fragments for longer duration and to determine the (final) mass and real size of the fragment. Thus, it should be noted that we can safely estimate the mass and size of the circumstellar disk before fragmentation, while they may somewhat change after fragmentation in the calculation with a much higher spatial resolution, or with the sink cells.

3.1.2. Cloud with $\beta_0 = 10^{-2}$

Figure 4 shows the time sequence for the model with $\beta_0 = 10^{-2}$ (model 3). Similar to the model with $\beta_0 = 10^{-3}$ (model 6), this model also shows the disk-like structure (i.e., disk-like first core) preceding the protostar formation (Figure 4(a)). Owing to the larger initial angular momentum, the first core in model 3 ($\beta_0 = 10^{-2}$) has a flatter structure than that in model 6 ($\beta_0 = 10^{-3}$). For this model, at the protostar formation epoch, the protostar has a mass of $M_{ps} \simeq 10^{-3} M_\odot$, while the disk has a mass of $M_{disk} \simeq 0.1 M_\odot$. Thus, the disk is about 100 times more massive than the protostar. Nevertheless, the circumstellar disk shows no fragmentation, as shown in Figures 4(b)–(d). Instead, the spiral structures appear with the gravitational instability in the circumstellar disk. The circumstellar disk extends up to ~ 500 AU (Figure 5(d)) by the epoch at which almost all gas in the host cloud has accreted onto the protostar and circumstellar disk system. By this epoch, the masses of protostar and circumstellar disk reach $M_{ps} = 0.35 M_\odot$ and

$M_{disk} = 0.58 M_\odot$, respectively. Thus, even at end of the main accretion phase, the circumstellar disk is more massive than the protostar. The disk properties and fragmentation condition are discussed in Section 4.1.

3.2. Disk Properties Versus Initial Rotational Energies

In this section, to investigate the disk properties, four different models with different initial rotational energies β_0 are presented. Figure 5 shows the density and velocity distribution for models with $\beta_0 = 10^{-2}$, 10^{-3} , 10^{-4} , and 10^{-5} at $t_c \simeq 10^5$ yr after the protostar formation. Since the free-fall timescale at the center of the initial cloud is $t_{ff,0} = 2.3 \times 10^4$ yr, there are structures at $\sim 4.3 t_{ff,0}$ after the protostar formation. The figure shows a larger disk with a larger β_0 . In addition, two clumps formed by fragmentation due to gravitational instability appear in the circumstellar disk for models with $\beta_0 = 10^{-3}$ and 10^{-4} , while no clump appears by the end of the main accretion phase for models with $\beta_0 = 10^{-2}$ and 10^{-5} . The fragmentation condition depends on the size and mass of the circumstellar disk (see Section 4.1).

Figure 6 shows the evolution of the disk mass before (left panel) and after (right panel) the protostar formation for the same models as in Figure 5. Note that the disk mass includes the mass of fragments after fragmentation. The figure indicates that the rotating disk forms before the protostar formation (i.e., $t_c < 0$) and has a mass of (6×10^{-3}) – $0.1 M_\odot$ at the protostar formation epoch. After the protostar forms, the circumstellar disk gradually increases its mass by gas accretion and reaches $M_{disk} = 0.1$ – $0.6 M_\odot$ by the end of the main accretion phase. The mass accretion rate onto the circumstellar disk during the main accretion phase ($\sim 10^5$ yr) is $\dot{M}_{disk} = (1$ – $5) \times 10^{-6} M_\odot \text{ yr}^{-1}$. This rate is determined by the balance between the mass accreting onto the circumstellar disk and mass infalling onto the protostar.

Figure 7(a) plots a time sequence of the residual mass $M_{res} = M_{ini} - M_{disk} - M_{ps}$ for the same models as in Figure 5, where M_{ini} is the initial mass of the host cloud (i.e., the mass inside $r < R_c$ in the initial cloud). The figure shows that the residual mass rapidly decreases in a free-fall timescale and reaches $\sim 0.1 M_\odot$ in $\sim 10^5$ yr. Thus, about 90% of the total mass accretes onto the protostar and circumstellar disk system by this epoch (see also Table 1). Therefore, the gas accretion almost halts and the main accretion phase ends at $t_c \sim 10^5$ yr.

Figure 7(b) shows the time evolution of the protostellar mass for the same models. The protostar has a mass of $(1$ – $3) \times 10^{-3} M_\odot$ at its formation epoch. Then, the protostar acquires its mass by gas accretion and reaches 0.3 – $0.9 M_\odot$ by the end of the main accretion phase. The mass accretion rate onto the protostar during the main accretion phase is $\dot{M}_{ps} = (3$ – $9) \times 10^{-6} M_\odot \text{ yr}^{-1}$ on average. The time variability of the mass accretion rate is shown in Section 3.3. Figures 6 and 7(b) indicate that the model with a larger rotational energy has a larger \dot{M}_{disk} , but smaller \dot{M}_{ps} . As shown in Figure 5, the cloud with a larger β_0 has a larger (or massive) rotating disk. In such a disk, the mass accretion onto the protostar is suppressed owing to larger angular momentum, and a less massive protostar appears with a relatively smaller protostellar accretion rate.

Figure 8 shows the disk-to-protostellar mass ratio μ against the protostellar mass for the same models as in Figure 5. The figure indicates that the circumstellar disk mass exceeds protostellar mass at the protostar formation epoch even for the model with a considerably small rotational energy. The cloud with larger rotational energy has a relatively massive

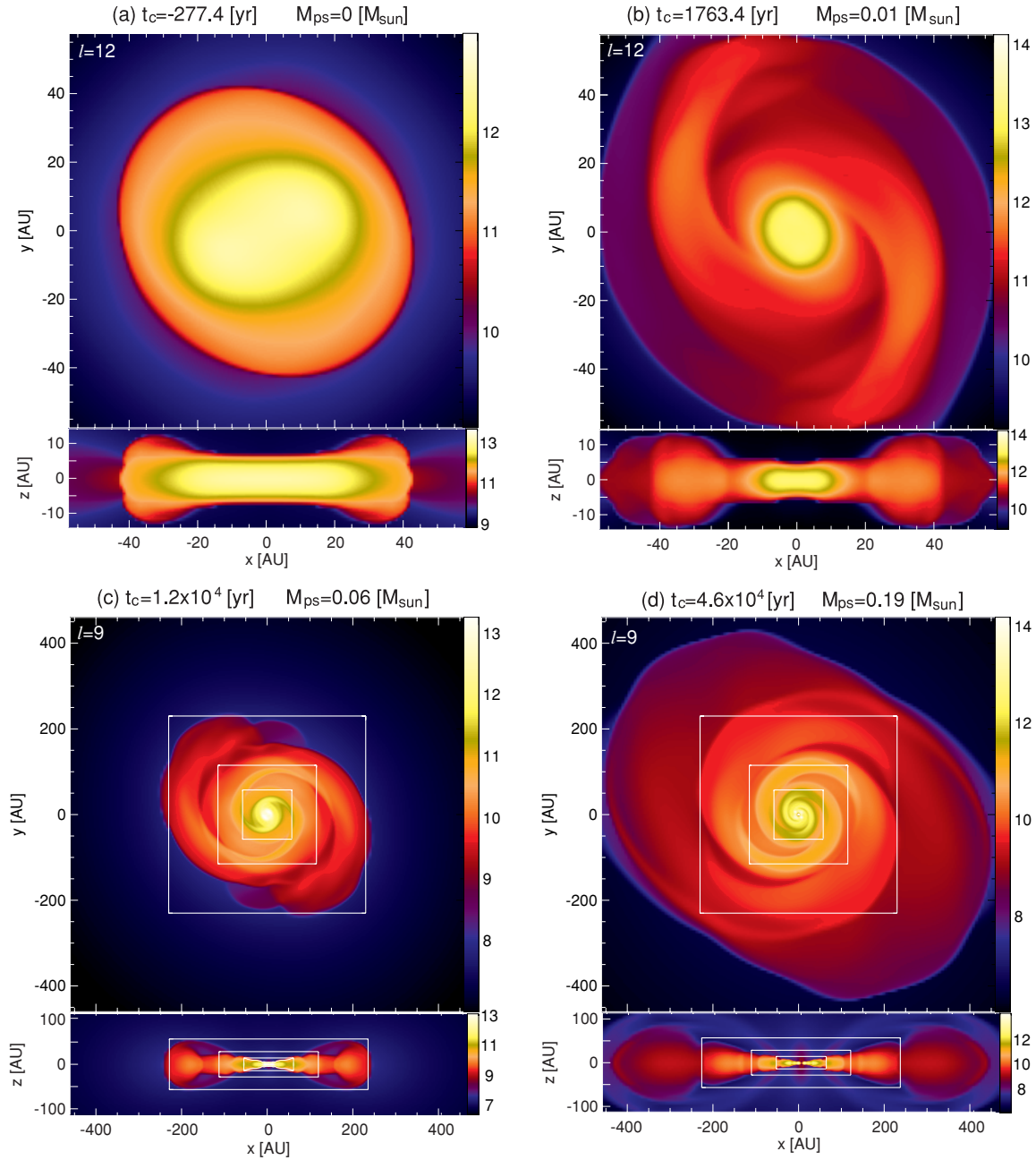


Figure 4. Density distributions (color scale) for model 3 ($\beta_0 = 10^{-2}$) are plotted on the cross section of the $z = 0$ (each upper panel) and $y = 0$ (each lower panel) planes. The grid scale of lower panels is eight times as large as that of upper panels. The time elapsed after the protostar formation (t_c) and the protostellar mass (M_{ps}) are shown in the upper side of each panel.

(A color version of this figure is available in the online journal.)

circumstellar disk at the protostar formation epoch. For example, the circumstellar disk for the model with $\beta_0 = 10^{-2}$ is about 100 times more massive than the protostar ($\mu = 100$), while for the model with $\beta_0 = 10^{-5}$ it is twice as massive ($\mu = 2$). The circumstellar disk is more massive than the protostar for most of the main accretion phase, except for the model with $\beta_0 = 10^{-5}$. In addition, the circumstellar disk mass even at the end of the main accretion phase for models with $\beta_0 \geq 10^{-4}$. Moreover, even in a cloud with $\beta_0 = 10^{-5}$ whose value is much smaller than the average of the observation $\beta_0 = 0.02$ (Caselli et al. 2002), the circumstellar disk has 1/10 ($\mu = 0.1$) of the protostellar mass at the end of the main accretion phase. Note that, as mentioned in

Section 3.1.1, our calculation may not have sufficient spatial resolution to investigate further evolution of fragments, and thus the disk-to-protostellar mass ratio after fragmentation may change when a higher spatial resolution or sink cell is adopted around fragments.

Figure 7(c) plots the evolution of the circumstellar disk radius after the protostar formation. The figure shows that the circumstellar disk with the radius of 3–40 AU already exists at the protostar formation epoch (i.e., $t_c = 0$). The size of the circumstellar disk increases with time and reaches 30–500 AU by the end of the main accretion phase. The figure also indicates that the protostar has a larger circumstellar disk for the cloud with larger β_0 .

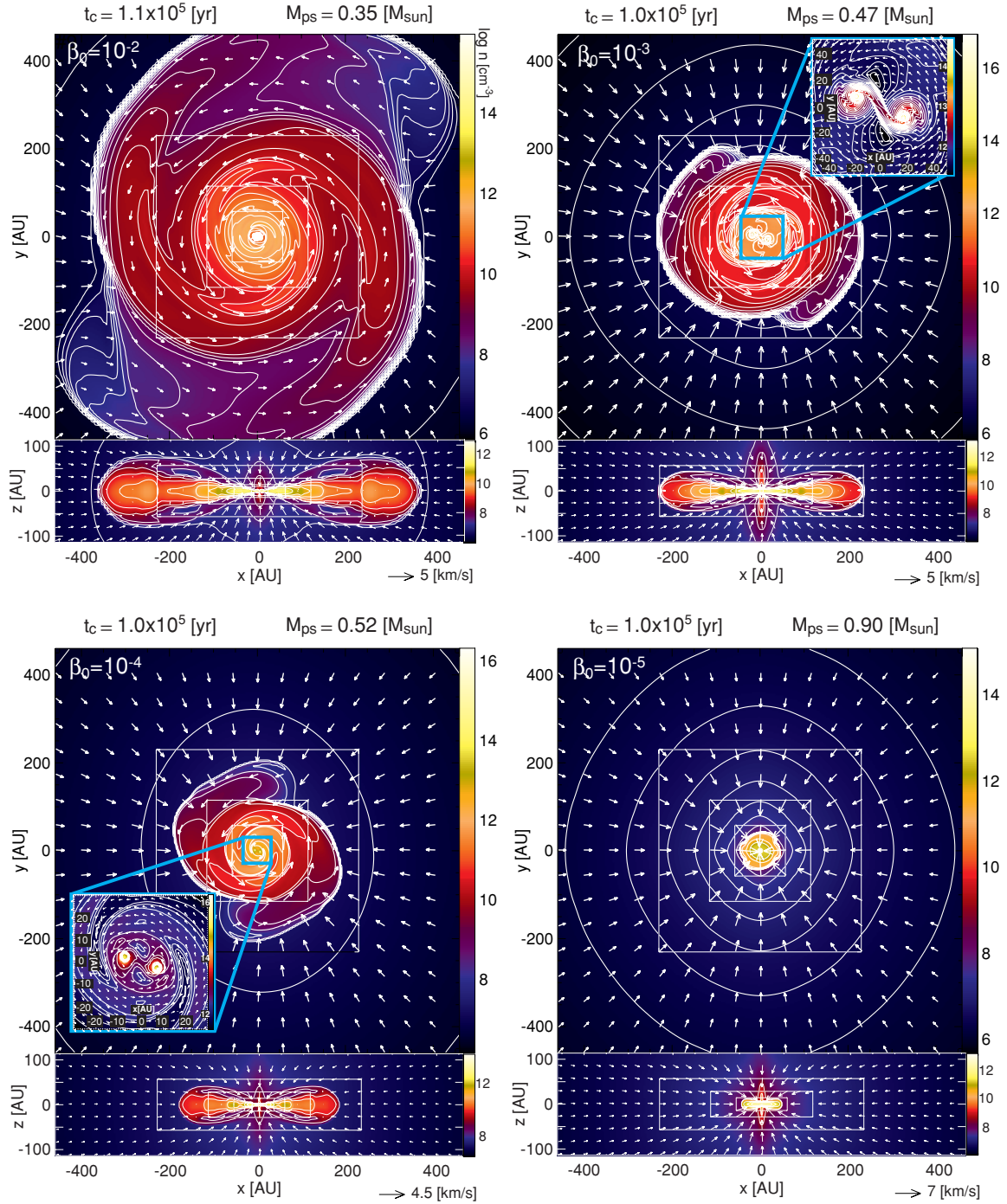


Figure 5. Final states on the cross section of $z = 0$ for models with $\beta_0 = 10^{-2}$ (model 3), 10^{-3} (model 6), 10^{-4} (model 8), and 10^{-5} (model 10). The density (color scale and contours) and velocity (arrows) distributions on the equatorial ($z = 0$) plane are plotted. The time elapsed after the protostar formation (t_c) and protostellar mass (M_{ps}) are shown in the upper side of each panel. The close-up view of the central region is plotted for models showing disk fragmentation.

(A color version of this figure is available in the online journal.)

Figure 7(d) plots the aspect ratio of the circumstellar disk, H/R , which is defined as $H/R \equiv h_z/(h_l h_s)^{1/2}$, and where h_l , h_s , and h_z are, respectively, lengths of the major axis, minor axis, and z -axis derived from the moment of inertia inside the circumstellar disk (see Machida et al. 2005b). Note that since h_l , h_s , and h_z are weighted by the mass, they are slightly different from the real size of the circumstellar disk which is surrounded by the accretion shock as shown in Figures 1 and 2. The figure shows that, for models with $\beta_0 < 10^{-2}$, the protostars have relatively thick circumstellar disks with $H/R > 0.5$ at their formation epochs

as also seen in Figure 2(c). On the other hand, for the model with $\beta_0 = 10^{-2}$, the protostar at its formation already has a thin circumstellar disk with $H/R < 0.2$. However, in any model, the aspect ratio decreases with time and reaches $H/R < 0.1$ by the end of the main accretion phase. Thus, protostars have a sufficiently thin disk at the end of the main accretion phase.

3.3. Mass Accretion Rate onto the Protostar

Figure 9 shows the mass accretion rate onto the protostar \dot{M}_{ps} (left axis) and the circumstellar disk mass (right axis)

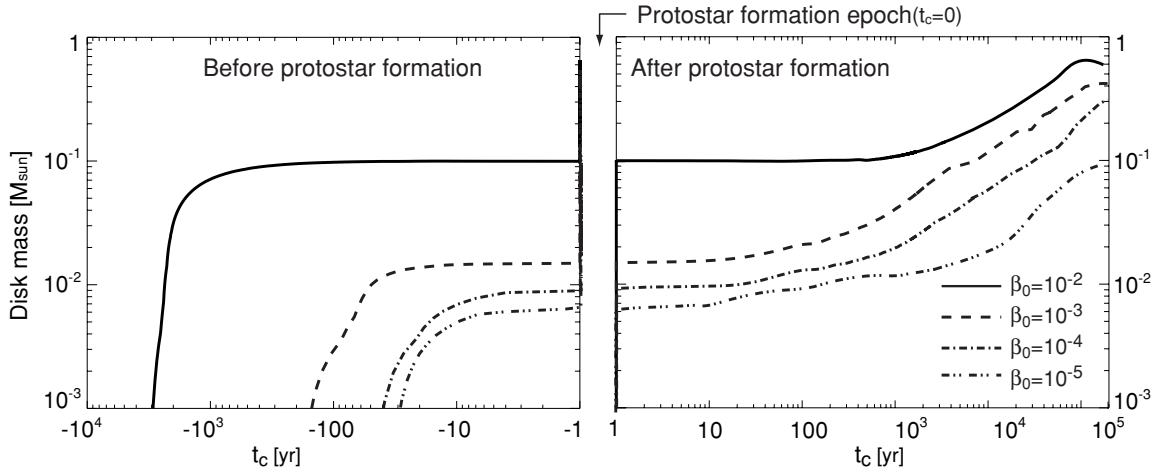


Figure 6. Evolution of the disk mass as a function of time before (left) and after (right) the protostar formation for models with $\beta_0 = 10^{-2}$ (model 3), 10^{-3} (model 6), 10^{-4} (model 8), and 10^{-5} (model 10).

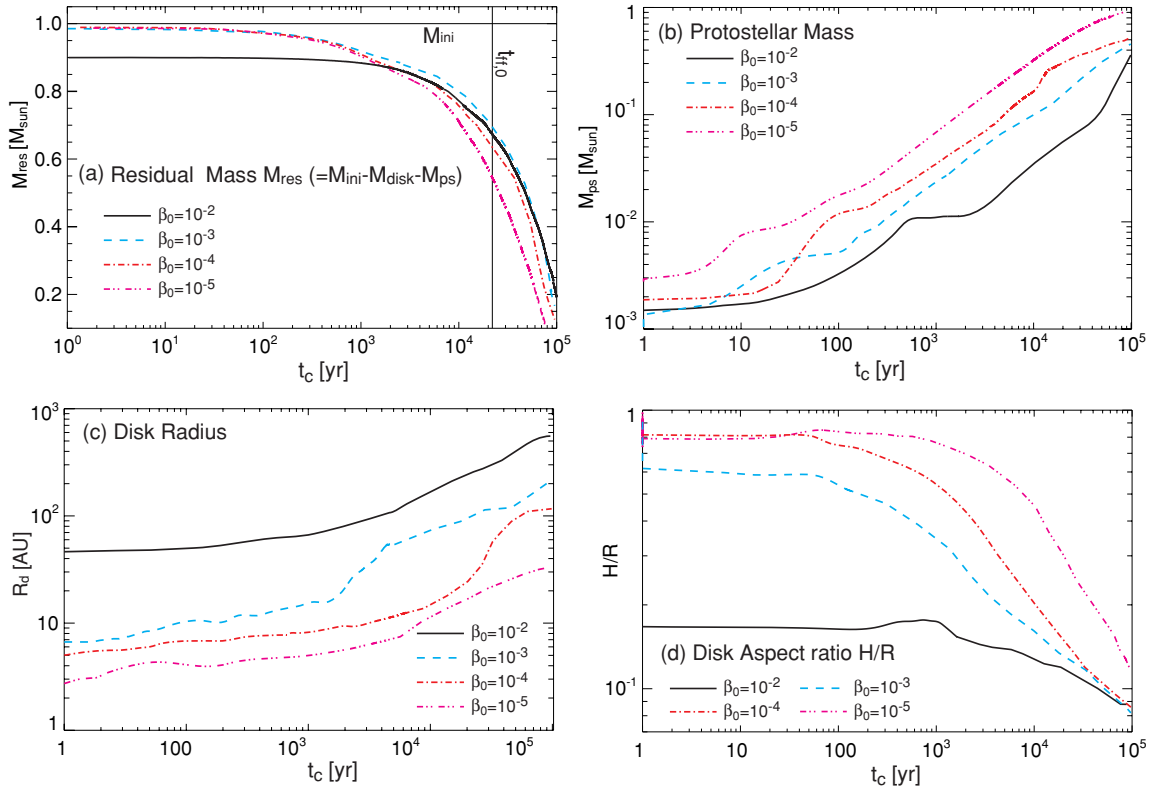


Figure 7. Evolution of (a) residual mass, $M_{\text{res}} \equiv M_{\text{ini}} - M_{\text{disk}} - M_{\text{ps}}$, (b) protostellar mass, M_{ps} , (c) disk radius R , and (d) aspect ratio of the disk H/R against time elapsed after the protostar formation for models with $\beta_0 = 10^{-2}$ (model 3), 10^{-3} (model 6), 10^{-4} (model 8), and 10^{-5} (model 10).

(A color version of this figure is available in the online journal.)

against the protostellar mass. As described in Section 2.1, we removed the gas having a number density of $n > 10^{13} \text{ cm}^{-3}$ in the region $r < 1 \text{ AU}$ from the computational domain. We regard the removed gas as the accreting mass onto the protostar and estimated the mass accretion rate in each step. The figure shows that the accretion rates are in the range of $10^{-4} \lesssim \dot{M}_{\text{ps}}/(M_{\odot} \text{ yr}^{-1}) \lesssim 10^{-6}$ in each model. In the simplified analysis based on self-similar solutions, the mass accretion rate is prescribed as $\dot{M} = f c_s^3/G$, where f is a numerical factor (e.g., $f = 0.975$ for Shu 1977; $f = 46.9$ for Hunter 1977). According to this, with temperature $T = 10 \text{ K}$ ($c_s = 0.2 \text{ km s}^{-1}$), the accretion rate in the main accretion phase is estimated to

be $\dot{M} = (2\text{--}90) \times 10^{-6} M_{\odot} \text{ yr}^{-1}$. Thus, the time averages of the accretion rates observed in our calculations correspond well to the theoretical expectation. Note, however, that the gas falls onto the protostar through the circumstellar disk, which is not taken into account in the model with self-similar solutions. Also note that the accretion rate shows a strong time variability as the protostellar and circumstellar mass increases. The rough accordance in the mass accretion rates of the simplified model and detailed numerical simulation indicates that the gravitational torque in the disk regulates the mass accretion onto the central star with the mass accretion from the envelope onto the disk.

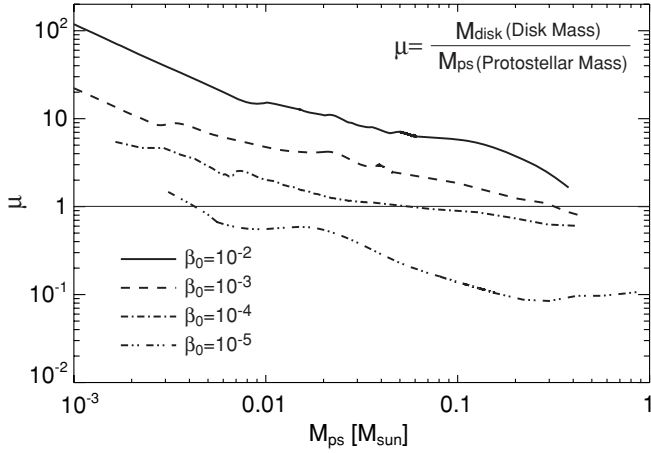


Figure 8. Evolution of the ratio of disk mass to protostellar mass against the protostellar mass for models with $\beta_0 = 10^{-2}$ (model 3), 10^{-3} (model 6), 10^{-4} (model 8), and 10^{-5} (model 10).

As shown in Figure 9, for models with $\beta_0 < 10^{-2}$, the accretion rate monotonically decreases initially, while it strongly fluctuates with time later as the protostellar (or circumstellar) mass increases. In addition, models with $\beta_0 = 10^{-2}$ show a strong time variability of the accretion rate right after the protostar formation. This time variability stems from spiral arms or clumps caused by the gravitational instability in the circumstellar disk. The epoch at which the accretion rate begins to fluctuate corresponds to the formation epoch of the spiral arm or clump. For example, for the model with $\beta_0 = 10^{-3}$, the accretion rate shows a slight time variability when $M_{ps} \lesssim 0.04 M_\odot$ (see Figures 1(c) and (d)), while it shows a strong variability when $M_{ps} \gtrsim 0.04 M_\odot$ (see Figures 1(e) and (f)). Indeed, when $M_{ps} \gtrsim 0.04 M_\odot$, the snapshot shows a spiral structure. Thus, this time variability of the mass accretion rate onto the protostar is closely related to the stability of the disk. We discuss the disk stability in Section 4.1.

4. DISCUSSION

4.1. Stability and Fragmentation Condition for Circumstellar Disks

As shown in Section 3, the circumstellar disk has a mass larger than or comparable to the protostellar mass in the main accretion phase. Such a massive disk tends to show fragmentation or the formation of spiral structure that is closely related to the mass accretion onto the central star, the subsequent evolution of the circumstellar and protoplanetary disk, and planet formation. In this section, we discuss the disk stability and fragmentation condition.

As shown in Figure 5, for typical models (models 3, 6, 8, and 10), fragmentation occurs in clouds with moderate rotational energies of $\beta_0 = 10^{-3}$ and 10^{-4} , while spiral arms appear without fragmentation in models with the larger ($\beta_0 = 10^{-2}$) and smallest ($\beta_0 = 10^{-5}$) rotational energies. To investigate the fragmentation condition of the disk, we calculated Toomre's Q parameter (Toomre 1964), which is defined as

$$Q = \frac{c_s \kappa}{\pi G \Sigma}, \quad (8)$$

where c_s , κ and Σ are the sound speed, the epicyclic frequency, and the surface density, respectively. We also calculated the ratio of the critical Jeans length λ_{cri} to the disk radius r_d (Matsumoto & Hanawa 2003) as

$$R_c = \frac{\lambda_{\text{cri}}}{r_d}, \quad (9)$$

where the critical Jeans length can be described as

$$\lambda_c = \frac{2c_s^2}{G\Sigma} [1 + (1 - Q)^{1/2}]^{-1}. \quad (10)$$

It is considered that fragmentation occurs when both conditions of $Q < 1$ and $R_c < 1$ are fulfilled in the disk. At each time

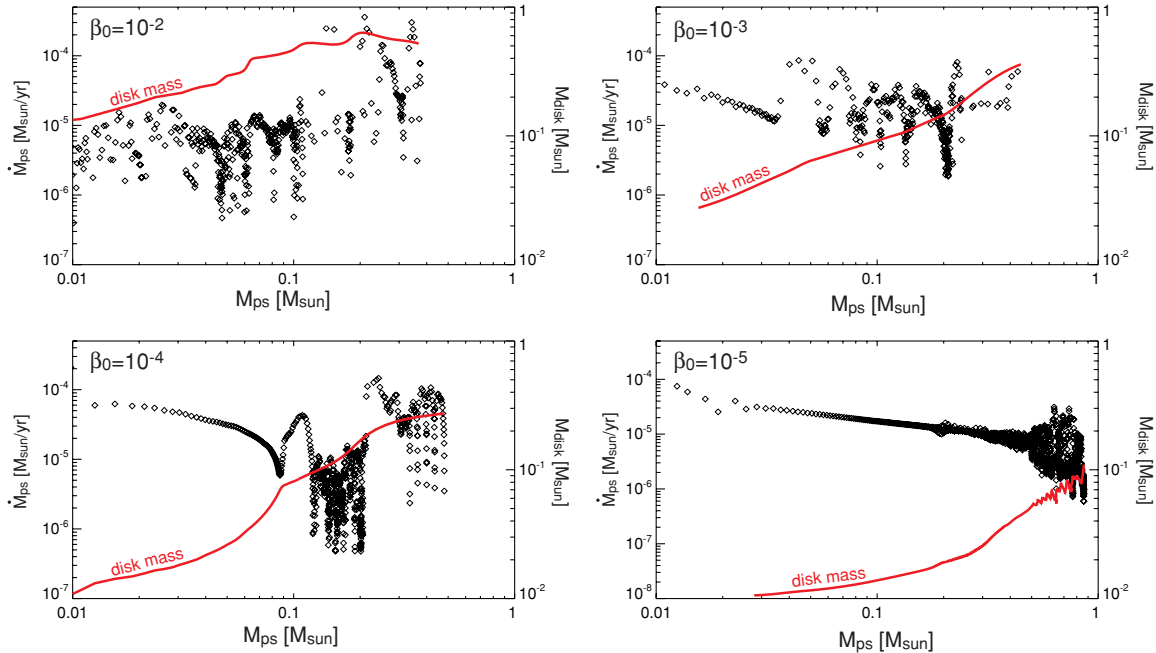


Figure 9. Mass accretion rate (left axis) and disk mass (right axis) are plotted for models 3, 6, 8 and 10. Note highly time-dependent \dot{M}_{ps} driven by gravitational torque due to non-axisymmetric structure in the disk.

(A color version of this figure is available in the online journal.)

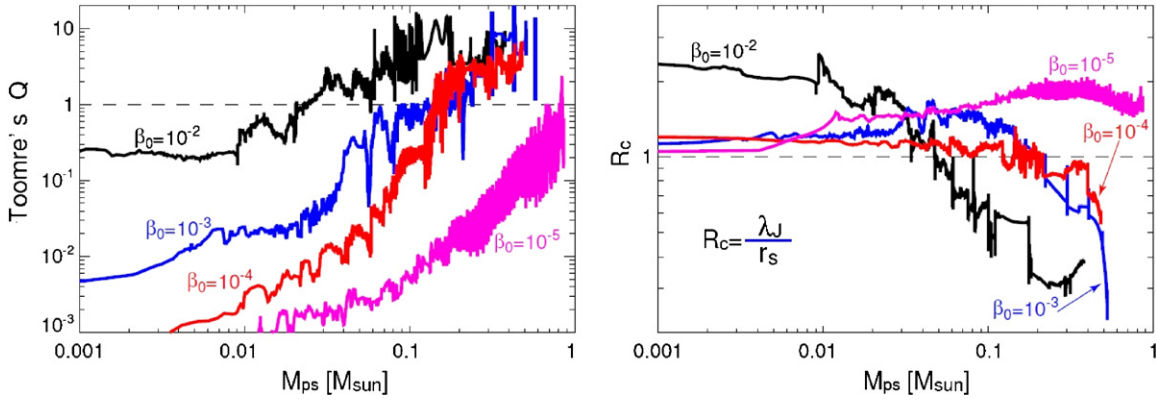


Figure 10. Averaged Toomre's Q (left panel) and the ratio of the critical Jeans length to disk radius (right panel) against the protostellar mass for models 3, 6, 8 and 10. (A color version of this figure is available in the online journal.)

step, we estimated Q and λ_c in each cell inside the disk (for a detailed description, see Matsumoto & Hanawa 2003). Then, these values are averaged within the whole disk to roughly estimate their time variability. Although we may have to measure local values of Q and R_c instead of global (or averaged) values for the investigation of the disk stability (Kratter et al. 2010), we use global values to roughly estimate the time evolution of the disk stability just for simplicity. In Figure 10, although we plotted Q from the epoch just after the protostar formation, the disk is not sufficiently thin in the early main accretion phase (see Figure 7(d)) and the Q criterion may not be applicable in a precise sense. However, the circumstellar disk becomes sufficiently thin with time and Q is safely applicable for $t_c \gtrsim 10^4$ yr when fragmentation occurs.

As shown in Section 3, the circumstellar disk originates from the first core that is formed in the early collapse phase. The first core is formed after the gas becomes adiabatic in the collapsing cloud core. Thus, the first core is mainly supported by the thermal pressure gradient force at its formation. Even when the initial host cloud has a significant rotational energy, the rotational energy of the first core is, at most, only 10% of the gravitational energy (Machida et al. 2005b, 2006). Then, the gas having a larger angular momentum accretes onto the disk (the first core or circumstellar disk) from the outer envelope as time goes on, and the disk gradually thins owing to the centrifugal force, and spreads out to a larger extent. Thus, it is considered that Q increases with time, because the gas with the larger specific angular momentum accretes onto the circumstellar disk with time; the epicyclic frequency or the ratio κ/Σ is expected to become large with time. Figure 10 (left panel) plots a time sequence of the averaged Q . The figure shows that, for any model, Q is much less than unity ($Q \ll 1$) at the protostar formation epoch and increases with time (or the protostellar mass). Finally, it reaches order unity, $Q \sim 1$, by the end of the main accretion phase in any model. The figure also shows that the circumstellar disk has a smaller Q in the cloud with smaller rotational energy. This is because, for the model with smaller β_0 , the gas with smaller specific angular momentum forms a disk.

In general, fragmentation can occur in the rotating disk with $Q < 1$. However, for the model with $\beta_0 = 10^{-2}$, although the circumstellar disk has $Q < 1$ when the protostellar mass is less than $M_{ps} < 0.02 M_\odot$, fragmentation does not occur, as shown in Figure 4. This is because the disk radius is smaller than the critical Jeans length ($R_c > 1$) when $M_{ps} < 0.02 M_\odot$. On the other hand, for this model, the disk radius is larger than

the critical Jeans length $R_c < 1$ when the protostellar mass is larger than $M_{ps} > 0.4 M_\odot$, while fragmentation does not occur because the Q parameter exceeds unity, $Q > 1$, in this phase. As a result, by the end of the main accretion phase, this model shows no fragmentation, while the spiral structure appears as shown in Figure 4.

For the model with $\beta_0 = 10^{-3}$, the circumstellar disk has $Q < 1$ for $M \lesssim 0.2 M_\odot$, and the ratio R_c manages to reach $R_c < 1$ in this period. Therefore, fragmentation occurs to form two clumps as shown in Figures 1 and 2. Even in the model with $\beta_0 = 10^{-4}$, these two conditions ($Q < 1$ and $R_c < 1$) are fulfilled for $M_{ps} \lesssim 0.1 M_\odot$, and fragmentation occurs. On the other hand, the model with $\beta_0 = 10^{-5}$ has $Q < 1$ through the main accretion phase, while fragmentation does not occur. This is because the disk size is smaller than the critical Jeans length by the end of the main accretion phase.

To investigate the fragmentation condition in the main accretion phase, we calculated 10 models in total, as listed in Table 1. Figure 5 implies that the upper border of the rotational energy between fragmentation and non-fragmentation models exists in models between $\beta_0 = 10^{-2}$ and 10^{-3} . To determine the fragmentation condition in more detail, we show the final fate for models $\beta_0 = 3 \times 10^{-3}$, 5×10^{-3} and 3×10^{-2} in Figure 11. The figure indicates that fragmentation border exists in models between $\beta_0 = 3 \times 10^{-3}$ and 5×10^{-3} . Fragmentation occurs in the model with $\beta_0 = 3 \times 10^{-3}$, while fragmentation does not occur in the model with $\beta_0 = 5 \times 10^{-3}$. In addition, fragmentation occurs again in the model with $\beta_0 = 3 \times 10^{-2}$. Note that, for this model, we stopped calculation long before the end of the main accretion phase ($t_c = 2.8 \times 10^3$ yr) because fragments move outwardly and the Jeans criterion is violated. This model shows fragmentation in the early main accretion phase of $t_c = 2 \times 10^3$ yr (see, Table 1) because a sufficiently large disk is already formed in the early collapse phase (i.e., before the main accretion phase). Moreover, the model with $\beta_0 = 5 \times 10^{-2}$ shows fragmentation in the early collapse phase (i.e., before the protostar formation; see Table 1). The fragmentation process in the early collapse phase was reported in many past studies (e.g., Bodenheimer et al. 2000; Goodwin et al. 2007). In summary, the fragmentation condition derived in our simulation can be described as follows.

1. $\beta_0 > 3 \times 10^{-2}$: fragmentation in the early collapse phase,
2. $5 \times 10^{-3} < \beta_0 < 3 \times 10^{-2}$: no fragmentation in the main accretion phase (see caution below),

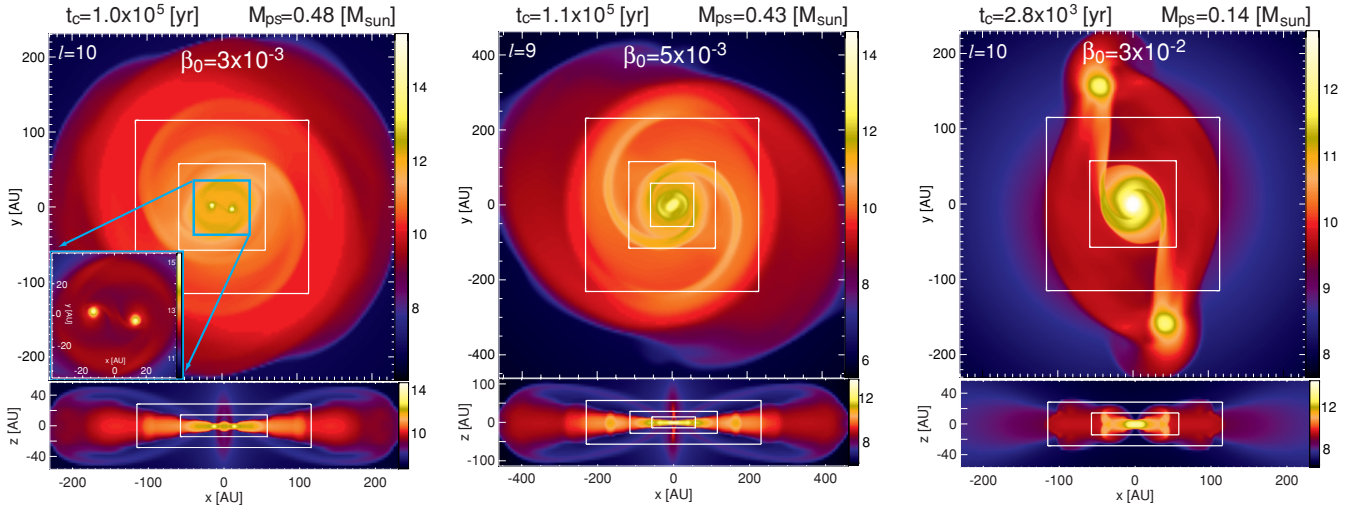


Figure 11. Final states on the cross section of $z = 0$ (each top panel) and $y = 0$ (each bottom panel) planes for models with $\beta_0 = 3 \times 10^{-3}$ (model 5), 5×10^{-3} (model 4) and 3×10^{-2} (model 2). The density distribution (color scale) is plotted in each panel. The time elapsed after the protostar formation (t_c) and protostellar mass (M_{ps}) are shown in the upper part of each panel.

(A color version of this figure is available in the online journal.)

3. $10^{-5} < \beta_0 < 5 \times 10^{-3}$: fragmentation in the main accretion phase,
4. $\beta_0 < 10^{-5}$: no fragmentation.

Although models having parameters of $5 \times 10^{-3} < \beta_0 < 3 \times 10^{-2}$ show no fragmentation, these models may show fragmentation in subsequent evolution stages. We calculated the disk evolution by the end of the main accretion phase in this study, while it is considered that the subsequent later phase of star formation before the main-sequence phase lasts for $\sim 10^7$ yr. As listed in Table 1, the mass of the circumstellar disk for the no fragmentation models is comparable to the protostellar mass at the end of the main accretion phase, in which Toomre's Q is nearly unity, $Q \sim 1$. Such a disk can fragment to form several clumps when the cooling timescale is shorter than the Kepler rotational timescale in the protoplanetary disk (Gammie 2001). In this study, we adopted a barotropic equation of state that makes the direct disk calculation from the molecular cloud until the end of the main accretion phase possible. In the main accretion phase, the mass of the circumstellar disk overwhelms the protostellar mass with $Q \ll 1$. In such a situation, it is expected that the cooling process is not so important for fragmentation. Instead, to investigate a marginal stable disk with $Q \sim 1$, the cooling process may be important (Durisen et al. 2007). Ideally, we should investigate the circumstellar disk formation from the molecular cloud core with radiative hydrodynamics, though we need to wait for further development of computational power to perform such calculations. Note that we added only $m = 2$ non-axisymmetric density perturbation to the initial state. Thus, the fragmentation condition derived in this study may change (only) quantitatively when other perturbation modes (especially $m = \text{odd number}$) are added to the initial state. However, we can expect that fragmentation in the circumstellar disk generally occurs because a massive circumstellar disk inevitably appears in the star formation process.

4.2. Implication for Planet Formation

As described in Section 4.1, a massive circumstellar disk inevitably appears in the main accretion phase. This is because

the first core that is a precursor of the circumstellar disk is about 10–100 times more massive than the protostar, reflecting the thermodynamics of the collapsing gas. Such a massive disk tends to show fragmentation owing to gravitational instability (Durisen et al. 2007). In our calculation, many models showed fragmentation and formation of small clumps in the circumstellar disk. As listed in Table 1, at the end of the calculation, fragments have a mass of $M_{\text{frag}} = (19\text{--}72) \times 10^{-3} M_{\odot}$ with a separation of $r_{\text{sep}} = 7.1\text{--}94.2$ AU. Note that the mass and separation of fragments may change to some degree if we include the effect of radiative cooling (see Section 4.5).

For every model, fragments survived without falling into the central protostar. Although the masses of fragments exist in the range of the brown dwarf ($M_{\text{frag}} = 13\text{--}75 M_{\text{Jup}}$), the planet-mass object may appear in the subsequent star formation phase, in which it is expected that the circumstellar disk cools to form less massive clumps (Durisen et al. 2007).

Recently, Neuhauser et al. (2005) observed a brown-dwarf mass companion around GQ Lup with a separation of ~ 100 AU. In 2008, direct images of planet mass companions around Fomalhaut (Kalas et al. 2008) and HR 8799 (Marois et al. 2008) are shown, in which they have masses of $3\text{--}10 M_{\text{Jup}}$ with separations of $24\text{--}98$ AU. It is considered that there are two different ways to form planets in the circumstellar (or protoplanetary) disk: one is via core accretion (Hayashi et al. 1985) and the other is via gravitational instability (Cameron 1978). In the core accretion scenario, it is difficult to account for the formation of massive planet in the region far from the protostar ($r_{\text{sep}} \gtrsim 5\text{--}10$ AU) in the standard disk model (Perri & Cameron 1974; Mizuno et al. 1978; Hayashi et al. 1985). On the other hand, a massive planet can form even in the region far from the protostar by fragmentation due to gravitational instability when the disk is sufficiently massive (Boley 2009). In this study, we showed that, in the circumstellar disk, gravitationally bound clumps can form in the region of $r_{\text{sep}} > 5$ AU. In addition, our calculation indicates that the massive circumstellar disks comparable to or more massive than the protostar form in the main accretion phase when the rotational energy of the molecular cloud is comparable to the observations ($10^{-4} < \beta_0 < 0.07$; Caselli et al. 2002).

Thus, the gravitational instability scenario may be more common for the planet formation.

4.3. Effects of Magnetic Field

In this study, we ignored the magnetic field. The magnetic field plays an important role in both the early collapse and main accretion phases, and is related to the formation process of the star and circumstellar disk. For example, a large fraction of the cloud mass is blown away by the protostellar outflow that is driven by the Lorentz force from the circumstellar disk. Thus, the protostellar outflow is expected to be closely related to the star formation efficiency (Matzner & McKee 2000; Machida et al. 2009). The protostellar outflow is also related to the determination of the circumstellar disk mass (e.g., Inutsuka et al. 2010). In addition, in the circumstellar disk, the turbulence owing to the magneto-rotational instability (MRI; Balbus & Hawley 1991) contributes to the angular momentum transfer that is related to the mass accretion rate onto the protostar. Moreover, the magnetic field suppress fragmentation (Machida et al. 2005a; Machida et al. 2008; Hennebelle & Teyssier 2008) and the formation of the disk (Mellon & Li 2008, 2009; Duffin & Pudritz 2009; Hennebelle & Ciardi 2009).

However, even when the molecular cloud is strongly magnetized, the mass of the first core and protostar is, respectively, $M_{\text{disk}} \sim 0.01\text{--}0.1 M_{\odot}$ and $M_{\text{ps}} \sim 10^{-3} M_{\odot}$ (Machida et al. 2007). Thus, as in the case of an unmagnetized cloud, the circumstellar disk mass overwhelms the protostellar mass at the protostar formation epoch. This is because the mass and size of each object (first core and protostar) are determined by the thermodynamics of the collapsing gas (Masunaga & Inutsuka 2000). In the main accretion phase, however, the masses of the circumstellar disk and protostar in magnetized clouds may be different from those in unmagnetized clouds because the angular momentum is transferred by the magnetic effect such as magnetic braking, protostellar outflow, and MRI. We will investigate the circumstellar disk formation in a magnetized cloud in detail in a subsequent paper.

4.4. Comparison with Previous Studies

In this study, we investigated the evolution of the circumstellar disk with parameter β_0 using a grid-based simulation and showed the parameter range for fragmentation (see Section 4.1). Walch et al. (2009) also investigated the disk evolution with β_0 using the three-dimensional SPH simulation. They calculated the evolution of clouds with $1.5 \times 10^{-4} < \beta_0 < 5 \times 10^{-2}$ and showed that fragmentation occurs with $\beta_0 > 0.02$. There is a slight quantitative difference for the fragmentation condition; fragmentation occurs in the model with $\beta_0 = 10^{-4}$ in our study, while no fragmentation occurs in the model with $\beta_0 = 1.5 \times 10^{-4}$ in Walch et al. (2009). However, the difference is considerably small despite the difference in the computational methods.

Fragmentation in the adiabatic collapsing phase was investigated in Matsumoto & Hanawa (2003). They have found that fragmentation may occur when $\beta_0 > 2 \times 10^{-3}$, while we have not yet observed fragmentation in our models with $0.005 < \beta_0 < 0.03$. This is not surprising since Matsumoto & Hanawa (2003) showed that the fragmentation condition also depends on the initial perturbation, and fragmentation does not always occur even if $\beta_0 > 2 \times 10^{-3}$. Therefore, we expect that the final outcome of the cloud with $0.005 < \beta_0 < 0.03$ may depend on details of the initial perturbation.

Kratter et al. (2010) investigated disk formation using the isothermal equation of states. Since the initial setting of their

models is mostly different from ours, we cannot directly compare our results with theirs. However, two of their models with $\beta_0 = 0.02$ and 0.08 using similar settings (initially BE density profile) showed fragmentation, which might be an indication of agreement with our results.

4.5. Caution for Fragments and Numerical Settings

In this study, we have shown that the first core formed in the gas-collapsing phase becomes the circumstellar disk in the main accretion phase, and the disk tends to show the gravitational instability because the circumstellar disk is more massive than the protostar in the early main accretion phase. Thus, in some models, fragmentation occurs and substellar-mass objects appear in the circumstellar disk. Since we are using Cartesian cells and have put an $m = 2$ initial perturbation, density distribution remains symmetric with respect to the center. As shown in Section 2.2, we adopted the sink only at the center of the computational domain and did not implement the moving sink for fragments. With this setup, we can safely calculate the disk evolution until the fragmentation of the disk and creation of additional collapsing objects, because the density always has a peak at the center of the computational domain. The fragments hardly increase its density to exceed n_{thr} because the gas behaves adiabatically in the high-density region according to Equation (4), in which the effects of radiative cooling and dissociation of molecular hydrogen are not taken into account. This treatment may overestimate the size of the fragments and possibly underestimate the mass of the fragments owing to the overestimated thermal pressure. Thus, the masses and orbital radii of fragments described in Table 1 may change when we include a more realistic thermal evolution. Note, however, that the masses and sizes of fragments may still not be calculated correctly even if we adopt the moving sink cells, because such treatment underestimates the thermal pressure and internal angular momentum (i.e., spin) of fragments.

In this study, we adopted the barotropic equation of state (Equation (4)) as the thermal evolution, in which the gas behaves adiabatically around the fragments. This treatment tends to underestimate the gas accretion onto the fragment, because we tend to overestimate the thermal pressure of the gas around the fragment that may have a chance to be radiatively cooled down within the disk. On the other hand, the gas might excessively fall onto the fragment from the circumstellar disk if the sink cells are adopted as the fragment, because the modeling with sink cells tends to underestimate the thermal pressure. Therefore, after fragmentation, the circumstellar disk derived in the calculation with the barotropic equation of state may be more massive than that with the sink cells. This indicates that we need a more realistic thermal evolution to determine the circumstellar disk mass after fragmentation. The only way to correctly calculate the evolution of the fragments seems to be radiation-hydrodynamics simulations with a much higher spatial resolution, which is beyond the capability of present computational resources.

At last, we comment on the initial perturbation. In this study, we have only added “ $m = 2$ ” density perturbation and avoided the inclusion of “ $m = \text{odd number}$ ” perturbation. We expect that the qualitative evolution of the circumstellar disk does not depend much on the initial perturbation, because the disk properties such as mass and size are essentially determined by the (roughly axisymmetric) gas accretion in the main accretion phase and thermodynamics in the gas-collapsing phase. However, the number and masses of

fragments may change according to the change in the initial perturbations.

5. SUMMARY

To investigate the circumstellar disk formation and its properties, we calculated the evolution of the unmagnetized molecular clouds from the prestellar core phase until the end of the main accretion phase going through the protostar formation, using three-dimensional nested-grid simulation that covers both the entire region of the initial molecular cloud and sub-AU structure. We constructed 10 models using as parameter the cloud's initial rotational energy (β_0), in which the size (6.2×10^3 AU) and mass ($1 M_\odot$) of the initial molecular cloud are fixed, and calculated their evolution until about 90% of the host cloud mass accretes onto either the protostar or circumstellar disk (i.e., until the end of the main accretion phase). The following results are obtained.

1. *The first core is a precursor of the circumstellar disk.* In the collapsing cloud core, the first core forms at $n_c \sim 10^{11} \text{ cm}^{-3}$ with a size of $\gtrsim 3$ AU before the protostar formation. At its formation, the first core exhibits a thick disk-like configuration with an aspect ratio of $H/R \simeq 0.6\text{--}0.9$. Then, after the protostar formation, the first core gradually transforms into a considerably thin disk ($H/R < 0.1$) that corresponds to the circumstellar disk. Thus, the minimum size of the circumstellar disk (or the size of the youngest circumstellar disk) is ~ 3 AU which corresponds to the size of the first core at its formation. The circumstellar disk is mainly supported by the thermal pressure gradient force in the early collapse and early main accretion phases, and then it is mainly supported by the centrifugal force and becomes very thin in the later main accretion phase because the gas with a large angular momentum accretes onto it.
2. *The circumstellar disks are more massive than the protostars in the early main accretion phase.* The first core has a mass of $\sim 0.01\text{--}0.1 M_\odot$, while the protostar has a mass of $\sim 10^{-3} M_\odot$ at its formation. The mass of each object almost corresponds to the Jeans mass at its formation. The first core evolves directly into the circumstellar disk. Thus, at the protostar formation epoch, the circumstellar disk is inevitably more massive than the protostar: the circumstellar disk is about 10–100 times more massive than the protostar. After the protostar formation (i.e., in the mass accretion phase), the gas accretes onto the protostar through the circumstellar disk. Since a part of the accreting gas accumulates in the disk, not only the protostellar mass but also the circumstellar mass increases. The mass growth rate of the protostar is larger than that of the circumstellar disk in the main accretion phase. Nevertheless, reflecting the large initial mass ratio between the protostar and circumstellar disk at their formation, the circumstellar disk is more massive than the protostar in the main accretion phase, at least before fragmentation occurs in the circumstellar disk. After fragmentation, however, the mass of the circumstellar disk tends to decrease rapidly, because the gas in the circumstellar disk accretes not only onto the protostar but also onto the fragments.
3. *The mass accretion rate onto the protostar shows a strong time variability in the main accretion phase.* After fragments appear in the circumstellar disk, the mass accretion rate onto the protostar shows a strong time variability, because low-mass objects effectively transfer the angular mo-

mentum outwardly to promote gas accretion onto the protostar. In addition, the spiral arms also contribute to a strong time variability of the mass accretion rate. On the other hand, there is little time variability of the accretion rate in a cloud with considerably lower rotation energy ($\beta_0 = 10^{-5}$) in the initial state. In such a model, since neither clumps nor clear spiral patterns appear in the circumstellar disk, the angular momentum transport is not so effective in the present modeling without magnetic field. Thus, the variability of the accretion rate provides a useful signature for detecting the low-mass companions or exo-planets around very young protostars.

Numerical computations were carried out on NEC SX-9 at the Center for Computational Astrophysics, CfCA, of the National Astronomical Observatory of Japan, and on NEC SX-8 at the Yukawa Institute Computer Facility. This work was supported by the Grants-in-Aid from MEXT (20540238, 21740136).

REFERENCES

- Arquilla, R., & Goldsmith, P. F. 1986, *ApJ*, **303**, 356
 Balbus, S. A., & Hawley, J. F. 1991, *ApJ*, **376**, 214
 Bate, M. R. 1998, *ApJ*, **508**, L95
 Bodenheimer, P., Burkert, A., Klein, R. I., & Boss, A. P. 2000, in *Protostars and Planets IV*, ed. V. Mannings, A. P. Boss, & S. S. Russell (Tucson, AZ: Univ. Arizona Press), 675
 Boley, A. C. 2009, *ApJ*, **695**, L53
 Calvet, N., Hartmann, L., & Strom, S. E. 2000, in *Protostars and Planets IV*, ed. V. Mannings, A. P. Boss, & S. S. Russell (Tucson, AZ: Univ. Arizona Press), 377
 Cameron, A. G. W. 1978, *Moon Planets*, **18**, 5
 Caselli, P., Benson, P. J., Myers, P. C., & Tafalla, M. 2002, *ApJ*, **572**, 238
 Duffin, D. F., & Pudritz, R. E. 2009, *ApJ*, **706**, L46
 Durisen, R. H., Boss, A. P., Mayer, L., Nelson, A. F., Quinn, T., & Rice, W. K. M. 2007, in *Protostars and Planets V*, ed. B. Reipurth, D. Jewitt, & K. Keil (Tucson, AZ: Univ. Arizona Press), 607
 Dutrey, A., Guilloteau, S., & Ho, P. 2007, in *Protostars and Planets V*, ed. B. Reipurth, D. Jewitt, & K. Keil (Tucson, AZ: Univ. Arizona Press), 495
 Enoch, M. L., Corder, S., Dunham, M. M., & Duchêne, G. 2009, *ApJ*, **707**, 103
 Gammie, C. F. 2001, *ApJ*, **553**, 174
 Goodman, A. A., Benson, P. J., Fuller, G. A., & Myers, P. C. 1993, *ApJ*, **406**, 528
 Goodwin, S. P., Kroupa, P., Goodman, A., & Burkert, A. 2007, in *Protostars and Planets V*, ed. B. Reipurth, D. Jewitt, & K. Keil (Tucson, AZ: Univ. Arizona Press), 133
 Hayashi, C., Nakazawa, K., & Nakagawa, Y. 1985, in *Protostars and Planets II*, ed. D. C. Black & M. S. Matthews (Tucson, AZ: Univ. Arizona Press), 110
 Hennebelle, P., & Ciardi, A. 2009, *A&A*, **506**, L29
 Hennebelle, P., & Teyssier, R. 2008, *A&A*, **477**, 25
 Hunter, C. 1977, *ApJ*, **218**, 834
 Inutsuka, S., Machida, M. N., & Matsumoto, T. 2010, *ApJ*, **718**, L58
 Kalas, P., et al. 2008, *Science*, **322**, 1345
 Kratter, K. M., Matzner, C. D., Krumholz, M. R., & Klein, R. I. 2010, *ApJ*, **708**, 1585
 Larson, R. B. 1969, *MNRAS*, **145**, 271
 Machida, M. N., Inutsuka, S., & Matsumoto, T. 2007, *ApJ*, **670**, 1198
 Machida, M. N., Inutsuka, S., & Matsumoto, T. 2009, *ApJ*, **699**, L157
 Machida, M. N., Matsumoto, T., Hanawa, T., & Tomisaka, K. 2005a, *MNRAS*, **362**, 382
 Machida, M. N., Matsumoto, T., Hanawa, T., & Tomisaka, K. 2006, *ApJ*, **645**, 1227
 Machida, M. N., Matsumoto, T., Tomisaka, K., & Hanawa, T. 2005b, *MNRAS*, **362**, 369
 Machida, M. N., Tomisaka, K., Matsumoto, T., & Inutsuka, S. 2008, *ApJ*, **677**, 327
 Marois, C., Macintosh, B., Barman, T., Zuckerman, B., Song, I., Patience, J., Lafrenière, D., & Doyon, R. 2008, *Science*, **322**, 1348
 Masunaga, H., & Inutsuka, S. 2000, *ApJ*, **531**, 350
 Masunaga, H., Miyama, S. M., & Inutsuka, S. 1998, *ApJ*, **495**, 346
 Matsumoto, T., & Hanawa, T. 2003, *ApJ*, **595**, 913
 Matzner, C. D., & McKee, C. F. 2000, *ApJ*, **545**, 364
 Mellon, R. R., & Li, Z.-Y. 2008, *ApJ*, **681**, 1356

- Mellon, R. R., & Li, Z.-Y. 2009, [ApJ](#), **698**, 922
- Meyer, M. R., Backman, D. E., Weinberger, A. J., & Wyatt, M. C. 2007, in *Protostars and Planets V*, ed. B. Reipurth, D. Jewitt, & K. Keil (Tucson, AZ: Univ. Arizona Press), 573
- Mizuno, H., Nakazawa, K., & Hayashi, C. 1978, [Prog. Theor. Phys.](#), **60**, 699
- Najita, J. R., Carr, J. S., Glassgold, A. E., & Valenti, J. A. 2007, in *Protostars and Planets V*, ed. B. Reipurth, D. Jewitt, & K. Keil (Tucson, AZ: Univ. Arizona Press), 507
- Natta, A., Grinin, V., & Mannings, V. 2000, in *Protostars and Planets IV*, ed. V. Mannings, A. P. Boss, & S. S. Russell (Tucson, AZ: Univ. Arizona Press), 559
- Neuhäuser, R., Guenther, E. W., Wuchterl, G., Mugrauer, M., Bedalov, A., & Hauschildt, P. H. 2005, [A&A](#), **435**, L13
- Perri, F., & Cameron, A. G. W. 1974, [Icarus](#), **22**, 416
- Saigo, K., & Tomisaka, K. 2006, [ApJ](#), **645**, 381
- Shu, F. H. 1977, [ApJ](#), **214**, 488
- Stamatellos, D., Whitworth, A. P., Bisbas, T., & Goodwin, S. 2007, [A&A](#), **475**, 37
- Toomre, A. 1964, [ApJ](#), **139**, 1217
- Truelove, J. K., Klein, R. I., McKee, C. F., Holliman, J. H., II, Howell, L. H., & Greenough, J. A. 1997, [ApJ](#), **489**, L179
- Vorobyov, E. I. 2009, [ApJ](#), **704**, 715
- Vorobyov, E. I., & Basu, S. 2007, [MNRAS](#), **381**, 1009
- Walch, S., Burkert, A., Whitworth, A., Naab, T., & Gritschneider, M. 2009, [MNRAS](#), **400**, 13
- Watson, A. M., Stapelfeldt, K. R., Wood, K., & Ménard, F. 2007, in *Protostars and Planets V*, ed. B. Reipurth, D. Jewitt, & K. Keil (Tucson, AZ: Univ. Arizona Press), 523
- Whitehouse, S. C., & Bate, M. R. 2006, [MNRAS](#), **367**, 32